

Are narrow spatial aftershock zones specific to fluid-induced earthquakes?

Kamran Karimi¹ and Jörn Davidsen¹

¹University of Calgary

November 23, 2022

Abstract

Aftershock cascades play an important role in forecasting seismicity in natural and human-made situations. While their behavior including the spatial aftershock zone has been the focus of many studies in tectonic settings, this is not the case when fluid flows are involved. Using high-quality seismic catalogs, we probe earthquake-earthquake triggering in three settings influenced by fluids: *(i)* A natural swarm (Long Valley Caldera, California), *(ii)* *suspected* swarms in the Yuha Desert (California), and *(iii)* induced seismicity in Oklahoma and southern Kansas. All settings exhibit significant aftershock behavior highlighting the importance of secondary processes. The spatial aftershock zones scale with mainshock magnitude as expected based on the rupture length. While *(i)* and *(iii)* show a rapid decay beyond their rupture length, *(ii)* exhibits long-range behavior suggesting that fluid migration might not be the dominant mechanism. We also find that aftershock productivity might allow to distinguish between natural swarms and induced seismicity.

15 Abstract

16 Aftershock cascades play an important role in forecasting seismicity in natural and
 17 human-made situations. While their behavior including the spatial aftershock zone has
 18 been the focus of many studies in tectonic settings, this is not the case when fluid flows are
 19 involved. Using high-quality seismic catalogs, we probe earthquake-earthquake triggering in
 20 three settings influenced by fluids: *i*) A natural swarm (Long Valley Caldera, California), *ii*)
 21 *suspected* swarms in the Yuha Desert (California), and *iii*) induced seismicity in Oklahoma
 22 and southern Kansas. All settings exhibit significant aftershock behavior highlighting the
 23 importance of secondary processes. The spatial aftershock zones scale with mainshock
 24 magnitude as expected based on the rupture length. While *i*) and *iii*) show a rapid decay
 25 beyond their rupture length, *ii*) exhibits long-range behavior suggesting that fluid migration
 26 might not be the dominant mechanism. We also find that aftershock productivity might
 27 allow to distinguish between natural swarms and induced seismicity.

28 Plain Language Summary

29 While it is known that fluid injection operations can induce seismic activity, it has
 30 remained unclear how this activity compares to their natural counterpart, seismic swarms
 31 driven by natural fluid flows. The latter are typically characterized by the absence of a domi-
 32 nant event within the seismic sequence, while exhibiting other characteristics consistent with
 33 tectonic aftershock sequences and secondary triggering. Our analysis of high-quality seis-
 34 mic catalogs for both types of fluid-induced seismicity shows that both exhibit a significant
 35 amount of secondary processes leading to *spatially localized* event-event triggering. Yet, the
 36 seismic productivity, which refers to the average increase in the number of aftershocks with
 37 the magnitude of their trigger, is significantly higher in the induced setting. Both findings
 38 are of direct importance for earthquake forecasting and seismic hazard assessment.

39 1 Introduction

40 Fluid-induced seismicity typically refers to (minor) seismic events that (partially) in-
 41 volve fluid flows. Examples range from *natural* flows associated with rainfalls and volcanic
 42 eruptions to *human-made* contexts including wastewater injection wells, hydraulic fractur-
 43 ing, and geothermal power plants. Recently, *anthropogenic* sources have lead to an extraor-
 44 dinary surge of seismic activities in different parts of the United States (Ellsworth, 2013).
 45 The most extreme cases are reported in Oklahoma and Southern Kansas where most seismic
 46 events are potentially linked to large-scale wastewater disposals. The USG survey indicates
 47 that no more than five (tectonic) earthquakes per year with magnitude $m \geq 3$ had been
 48 previously reported over almost three decades (Deflandre, 2016), in sharp contrast to the
 49 one thousand $m \geq 3$ earthquakes recorded in 2016. In this context, it is essential to identify
 50 potential anthropogenic origins and relevant secondary triggering mechanisms, which has
 51 important consequences in terms of seismic hazard assessment, earthquake forecasting and
 52 effective mitigation strategies.

53 To what extent fluid-based anthropogenic seismicity bears similarities with its natu-
 54 ral analog is an open question. Swarm-like features of induced seismicity associated with
 55 wastewater disposal and/or hydraulic fracturing were found in (Skoumal et al., 2015). Signa-
 56 tures of event-event triggering or aftershock dynamics were recently reported in (Maghsoudi
 57 et al., 2016, 2018), where common features of event-event triggering and natural earthquake
 58 swarms, *i.e.* productivity relation or the Omori-Utsu (OU) relation as well as an absence of
 59 Båth's law, were recovered within the context of hydraulic fracturing-induced microseismic-
 60 ity. Recent studies point to pore-pressure fluctuations, poro-elastic effects, or combination
 61 of those two as relevant activation mechanisms (T. H. Goebel & Brodsky, 2018) as well
 62 as aseismic creep (Eyre et al., 2019). The signatures of event-event triggering in induced
 63 settings also indicate the relevance of static stress transfer, similar to the case of aftershocks

64 in tectonic settings (Maghsoudi et al., 2018). In general, the features of the spatio-temporal
 65 evolution of induced seismicity can be viewed as a main signature of the underlying physi-
 66 cal activation and secondary triggering processes. For example, the typical diffusion-based
 67 picture is that the activation takes place in a spatially *local* manner and over diffusion
 68 timescales giving rise to a square-root time dependence of the distance (Shapiro, 2015). On
 69 the other hand, the overall increase in the spatial extent of induced seismicity could be
 70 interpreted in terms of poro-elastic interactions between migrating fluids and embedding
 71 porous solids (T. H. Goebel & Brodsky, 2018).

72 To which degree the mechanisms are affected by the specific source — anthropogenic or
 73 natural sources — has remained largely unexplored. Here, our aim is to identify common-
 74 alities and differences in the spatio-temporal dynamics of induced and natural seismicity in
 75 fluid-driven situations. To this end, we analyzed aftershocks properties in *i*) Oklahoma and
 76 southern Kansas and compared our observations with two other case studies, which are *ii*)
 77 the Long Valley Caldera and *iii*) the Yuha Desert, whose seismic activities are believed to be
 78 strongly influenced by the natural migration of fluids. Our overall methodology is similar to
 79 the one used by Vasylykivska and Huerta (2017); Schoenball and Ellsworth (2017a) in Okla-
 80 homa and Kansas aiming to distinguish between background events (as a direct consequence
 81 of fluid injection) and triggered events (due to secondary mechanisms).

82 All settings exhibit a significant amount of event-event triggering highlighting the im-
 83 portance of secondary processes for the overall seismicity. The event-event triggering rates
 84 in *i*) exhibit similar temporal features to those of natural earthquakes in *ii*), *iii*) and can
 85 be quantified by the OU relation (Kagan, 2013). In all cases, the productivity relation
 86 between the total number of aftershocks and the triggers' magnitude also holds, yet the
 87 number of triggered events increases much more rapidly with magnitude for *i*). The spatial
 88 clustering of aftershocks in *i*) is quantified by a steep algebraic decay with distance beyond
 89 the rupture length of the main shock. This agrees closely with the narrow aftershock zones
 90 associated with natural swarms in *ii*) suggesting that short-ranged triggering is not specific
 91 to human-made contexts. Moreover, we find analogous *topological* features associated with
 92 triggering cascades in *i*) and *ii*) confirming the swarm-like nature of induced seismicity in
 93 the former. In *iii*), however, aftershock sequences tend to be *burst-like* and the aftershock
 94 zones extend well beyond the associated rupture size. In fact, the fluid diffusion may not be
 95 the dominant contribution in *iii*) and other mechanisms — such as non-local stress transfer
 96 and aseismic deformations — and/or the underlying fault network might be more relevant
 97 in this context.

98 2 Data

99 We analyze three different, previously published high-resolution seismic catalogs, for
 100 which fluids are thought to play a significant role in driving seismic activity. For the
 101 injection-induced seismicity in Oklahoma and southern Kansas, we use a relocated cat-
 102 alog (Schoenball & Ellsworth, 2017a, 2017b). The region witnessed an almost ten fold
 103 increase in the overall seismicity rate over two years, which declined later on due to scaling
 104 down of industrial operations (Langenbruch & Zoback, 2016). A magnitude 5.8 earthquake
 105 occurred during this mitigation period and led to a spontaneous increase in the seismic activ-
 106 ity indicating the significance of *secondary* triggering processes and aftershocks (Fig. S1(a)
 107 in SM). The Yuha Desert catalog (Ross et al., 2017) contains pronounced aftershock activity
 108 following the 2010 magnitude 7.2 El Mayor-Cucupah event (Fig. S1(b) in SM). We neglect
 109 the initial ten days after the event during which the seismic activity is mostly affected by
 110 aseismic deformations and instead, we focus on the later times, suggested to be driven by
 111 fluid diffusion (Ross et al., 2017). The Long Valley Caldera catalog (Shelly et al., 2016)
 112 corresponds to a five-month sequence of natural swarms (Fig. S1(c) in SM).

113 In all cases, the frequency-magnitude distributions largely follow the Gutenberg-Richter
 114 (GR) relation $N(\text{Mag.} > m) \propto 10^{-b(m-m_c)}$ (right panels of Fig. S1(a-c) in SM). Here, the

115 b -value controls the exponential decay rate and m_c denotes the magnitude of completeness.
 116 We vary m_{th} and include events with $m \geq m_{th}$ to estimate $b(m_{th})$ based on the maximum-
 117 likelihood estimator (Bhattacharya et al., 2011). We estimate both b and m_c by identifying
 118 the lowest value of m_{th} for which b becomes constant (Davidsen et al., 2015). For Oklahoma
 119 and southern Kansas (Fig. S1(a)), we obtain $b = 1.65$. The high b -value implies an exces-
 120 sive number of lower-magnitude earthquakes compared to tectonic settings, which typically
 121 exhibit $b \simeq 1$ (Kagan, 2013). Yet, similarly high b -values are observed for microseismic
 122 events associated with hydraulic fracturing (Eaton et al., 2014; Eaton & Maghsoudi, 2015;
 123 Maghsoudi et al., 2016; Dinske & Shapiro, 2013). For the Yuha Desert, we obtain $b = 0.95$
 124 (Fig. S1(b)). The Long Valley catalog (Fig. S1(c)) is lacking a unique b -value. Our analysis
 125 indicates two regimes with $b = 0.7$ for $m_c = 0.2$ and $b = 0.9$ for $m_c = 1.0$. Thus, we use
 126 both sets of parameters for our triggering analysis. Using two different estimators (Kantz &
 127 Schreiber, 2004; Gneiting et al., 2012), the spatial distribution of hypocenters can be well
 128 approximated as a fractal with a fractal dimension $d_f \simeq 2$ for all catalogs.

129 3 Methodology: Event-event triggering and aftershock identification

130 We follow the methodology first proposed by (Zaliapin et al., 2008), which allows for
 131 a robust classification between triggered events (aftershocks) and events not triggered by
 132 other events in the catalog, considered background events (Zaliapin et al., 2008; Gu et al.,
 133 2013; Zaliapin & Ben-Zion, 2013; Moradpour et al., 2014; Davidsen et al., 2015; Schoenball
 134 et al., 2015; Davidsen & Baiesi, 2016; Davidsen et al., 2017; Maghsoudi et al., 2018; Teng &
 135 Baker, 2019). The starting point is the GR relation, which is used to formulate an expected
 136 magnitude-dependent rate of activity for a spatially uniform and stationary Poisson process.
 137 This rate allows one to formulate the null hypothesis of independent events — correspond-
 138 ing to background events — and the method seeks for possible rejections of it to identify
 139 triggered events and their trigger. As a first step, the present approach associates each event
 140 j to a set of possible triggers $\{i\}$ with $(t_i < t_j, \vec{r}_i, m_i)$ that fulfill $r_{ij} \equiv |\vec{r}_i - \vec{r}_j| \leq c_p t_{ij}$ with
 141 $t_{ij} \equiv t_j - t_i$ and pressure wave velocity $c_p \simeq 6 \text{ km s}^{-1}$ to ensure causality (Moradpour et al.,
 142 2014). The pair-wise quantity $n_{ij} \equiv c_g t_{ij} r_{ij}^{d_f} 10^{-b(m_i - m_c)}$ gives the expected number of
 143 magnitude m_i events between events i and j . Here, the prefactor c_g relates to the regional
 144 seismicity rate. We can set $c_g = 1$ without loss of generality. The most likely trigger i^*
 145 of event j can be identified by $n_j^* = \min_i \{n_{ij}\}$, since it is the strongest possible violation
 146 of the null hypothesis. Low values of n_j^* can be associated with triggered events and high
 147 values can be associated with background events. The separation between these groups can
 148 be readily seen in a two-dimensional projection of n_j^* using (t_j^*, r_j^*) defined as

$$149 \quad \begin{aligned} t_j^* &\equiv t_{i^*j} 10^{-\frac{b}{2}(m_{i^*} - m_c)}, \\ r_j^* &\equiv r_{i^*j}^{d_f} 10^{-\frac{b}{2}(m_{i^*} - m_c)}, \end{aligned} \quad (1)$$

151 such that $n_j^* = r_j^* \times t_j^*$. Using the density distribution of n_j^* in this projection, one can
 152 choose a suitable threshold n_{th} for the separation (see SM for further discussion).

153 4 Results

154 Using the above methodology to identify event-event triggering, we find that all catalogs
 155 exhibit significant triggering and aftershocks (Fig. S2 in SM). This enables us to study the
 156 properties of the direct event-event triggering (the first generation of aftershocks) and their
 157 variations with time, distance, and magnitude.

158 4.1 Spatial aftershock zones

159 We evaluate the linear (normalized) aftershocks density $\rho_m(r)$ associated with triggers
 160 (or main shocks) of magnitude m . Displayed in the insets of Fig. 1(a-d), almost all after-
 161 shocks densities show an initial increase up to a peak followed by a power-law like decrease.

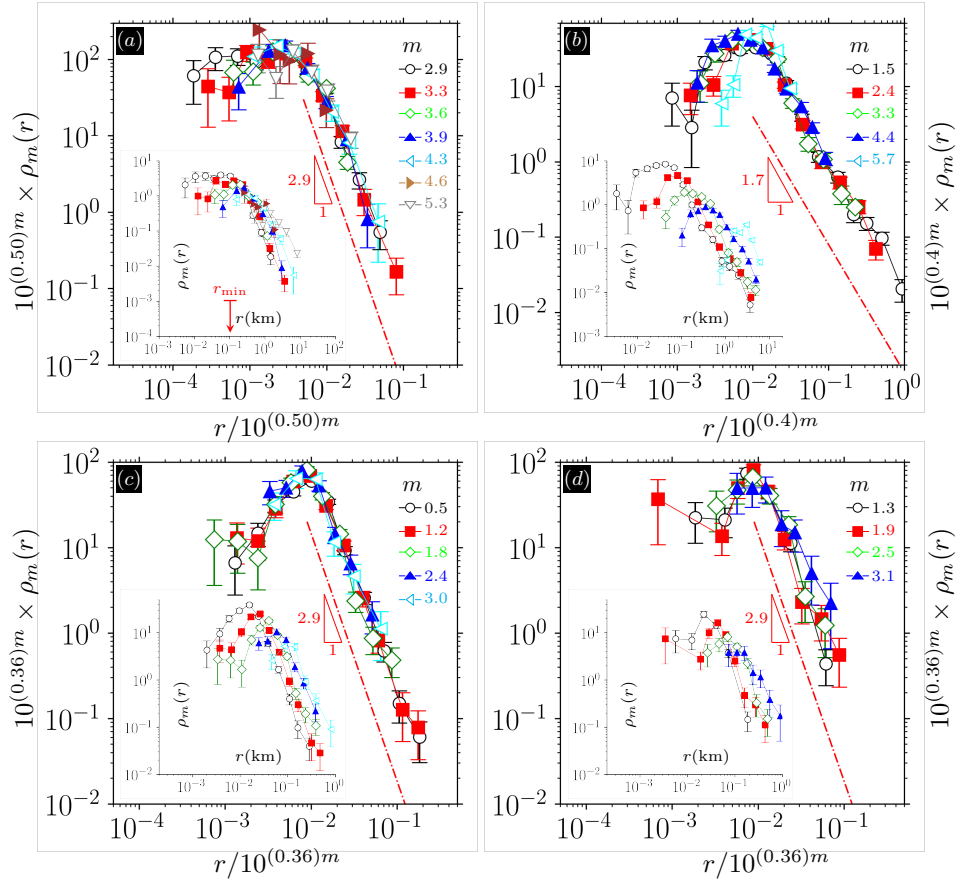


Figure 1. Rescaled probability density function of aftershocks $10^{\sigma m} \times \rho_m(r)$ against scaled distance $r/10^{\sigma m}$ in **a)** Oklahoma and southern Kansas **b)** the Yuha Desert **c)** Long Valley Caldera with $b = 0.7, m_c = 0.2$ **d)** Long Valley Caldera with $b = 0.9, m_c = 1.0$ conditioned based on the mean main shock magnitude m in a given range. The dash-dotted lines indicate $\rho(r) \propto r^{-\nu}$ for large r . The insets show the unrescaled data presented in the main plots. The red arrow indicates the average relative location uncertainty where available.

162 As for tectonic events (Gu et al., 2013), the location of the peak is closely aligned with the
 163 rupture length of the trigger, which scales as $r_{\text{rup}} \propto 10^{\sigma m}$. To test this explicitly, we rescale
 164 the distance r with $10^{\sigma m}$ and we indeed obtain a robust data collapse of all aftershock
 165 densities for a given catalog in Fig. 1(a-d). The variation between the different catalogs is
 166 minimal, namely $0.36 < \sigma < 0.5$, which is consistent with previously reported estimates for
 167 tectonic earthquakes (Leonard, 2010; Brengman et al., 2019; Moradpour et al., 2014). The
 168 data collapses also indicate that beyond the rupture length the aftershock density decays
 169 as $r^{-\nu}$. While aftershock zones in Oklahoma and southern Kansas as well as in the Long
 170 Valley Caldera exhibit a steep decay with $\nu \simeq 2.9$, the Yuha Desert data indicate a longer-
 171 ranged trend ($\nu \simeq 1.7$), typical of tectonic seismicity in southern California (Gu et al., 2013;
 172 Moradpour et al., 2014).

173 4.2 Aftershock productivity

174 We next focus on the variation of the number of triggered events or first generation
 175 of aftershocks N_{as} with the magnitude m of the trigger as displayed in Fig. 2. If averaged
 176 over triggers with the same m , we find an exponential scaling of the number of triggered

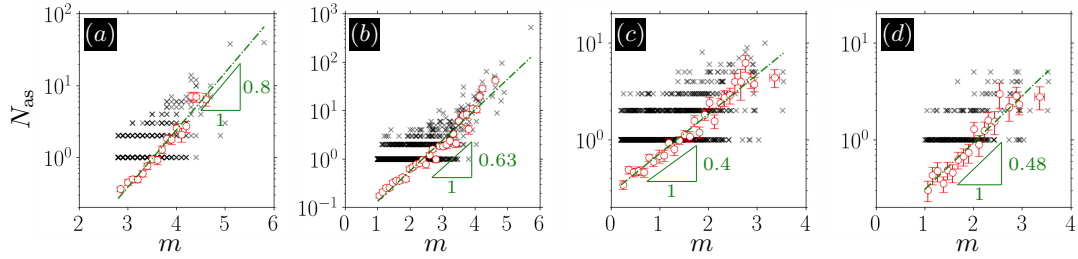


Figure 2. Number of aftershocks $N_{\text{as}}(m)$ as a function of trigger magnitude m in **a)** Oklahoma and southern Kansas **b)** the Yuha Desert **c)** Long Valley Caldera with $b = 0.7, m_c = 0.2$ **d)** Long Valley Caldera with $b = 0.9, m_c = 1.0$. The symbols ($-o-$) indicate the mean value \bar{N}_{as} over prescribed bins. The error bars denote the standard error. The dash-dotted line indicates the productivity relation $\bar{N}_{\text{as}} \propto 10^{\alpha m}$.

177 events with m in all cases, i.e., $N_{\text{as}} \propto 10^{\alpha m}$ as also observed in tectonic settings (Dascher-
 178 Cousineau et al., 2020). The scaling exponent α controls the rate of exponential growth with
 179 m and we find that the value of α varies between catalogs. We obtain $\alpha \simeq 0.8$ for Oklahoma
 180 and southern Kansas, while in the Yuha Desert $\alpha \simeq 0.63$, and $\alpha < 0.5$ in the Long Valley
 181 Caldera. This implies that the productivity of triggers or mainshocks increases faster with
 182 magnitude in Oklahoma and southern Kansas than in the other cases while being comparable
 183 to tectonic systems (Gu et al., 2013; Moradpour et al., 2014). Note that variations in α
 184 have recently been attributed to mainshock properties and associated variations in terms
 185 of focal mechanisms, amplitude of stress drops, and on-fault slip distributions (Dascher-
 186 Cousineau et al., 2020), which might be at play for the different catalogs here as well. Note
 187 also that $\alpha \simeq 1.1$ has been reported in (T. Goebel et al., 2019) for Oklahoma and southern
 188 Kansas using a different methodology. The specific criteria to define and identify aftershocks
 189 might be responsible for the differences (Hainzl et al., 2013) since they are known to lead
 190 to significant biases in the estimation (Marsan & Helmstetter, 2017; Marsan & Lengline,
 191 2008). In all cases, we find $\alpha < b$ implying that the overall event-event triggering budget is
 192 dominated by the more frequent smaller triggers instead of the fewer larger triggers (Gu et
 193 al., 2013).

194 4.3 Temporal aftershock rates

195 For a given event, the temporal rate of events it triggers varies with time. The insets of
 196 Fig. 3(a-d) display the daily aftershocks rates associated with triggers of magnitude m for our
 197 catalogs. In all cases, they follow approximately the OU relation $\lambda(t) = \frac{K}{(c+t)^p}$ over four to
 198 five decades, first established for tectonic earthquakes (Utsu et al., 1995; Davidsen & Baiesi,
 199 2016). Here, t denotes the time after the trigger or mainshock, c is a characteristic timescale
 200 — whose origin is still debated (Davidsen & Baiesi, 2016; Hainzl, 2016) — separating the
 201 constant rate regime from an algebraically decaying one with exponent p , and K determines
 202 the maximum rate. For all case, we find $p \approx 1$, similar to what has been observed for tectonic
 203 earthquakes (Gu et al., 2013; Scholz, 2019). It is known that the used methodology has by
 204 construction a tendency to underestimate the true aftershock rates at late times (Davidsen
 205 & Baiesi, 2016) explaining the noticeably faster decay in the rates close to their respective
 206 maximum duration. Comparing the triggering rates for different trigger magnitudes, there
 207 is a general trend that the rates increase with m . Indeed, provided that c and p do not
 208 vary with m and m_c is fixed, the aftershock productivity relation discussed above implies
 209 that on average $K \propto 10^{\alpha m}$. This is directly tested in Fig. 3(a-d) by plotting $\lambda_m(t)/10^{\alpha m}$
 210 against t . For all catalogs, we obtain a very good scaling collapse onto a master curve for
 211 almost all data. A noticeable exception is the rate for $m = 5.7$ in the Yuha Desert case,
 212 which corresponds to a *single* (and the largest) aftershock sequence and, thus, the deviation

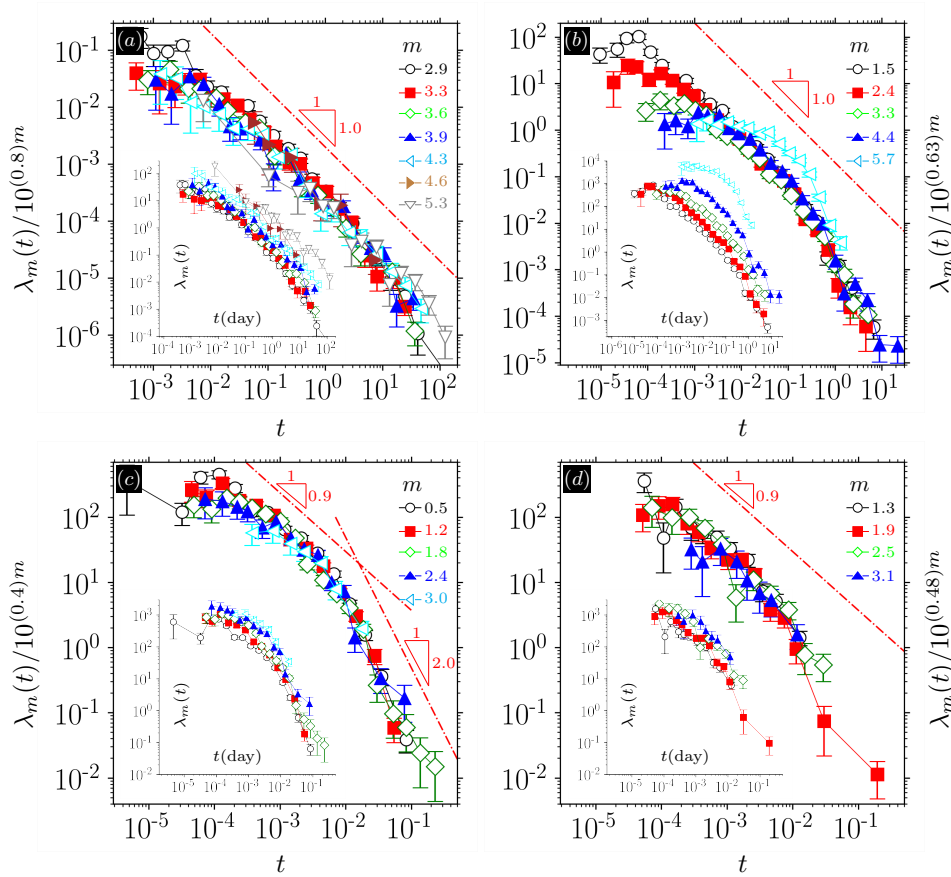


Figure 3. Rescaled aftershock rates $\lambda_m(t)/10^{\alpha m}$ versus time t in **a)** Oklahoma and southern Kansas **b)** the Yuha Desert, California **c)** Long Valley Caldera with $b = 0.7, m_c = 0.2$ **d)** Long Valley Caldera with $b = 0.9, m_c = 1.0$ for different mainshock magnitude ranges with mean magnitude m . Here, α denotes the productivity exponent as reported in Fig. 2. The (red) dash-dotted line indicates t^{-p} . The insets show the actual rates.

213 can likely be attributed to the natural variation in aftershock productivity discussed above.
 214 The scaling collapse on a master curve also shows that the Long Valley Caldera data in
 215 Fig. 3(c-d) may exhibit two different power-law regimes: an initial power-law with $p \simeq 1.0$
 216 at $t < 10^{-2}$ (day) followed by a more rapid decay with exponent $\simeq 2$. Such a behavior
 217 is reminiscent of what has been observed in rock fracture (Davidsen et al., 2017; Baró &
 218 Davidsen, 2017). Fig. 3(a-d) also shows that only for the Yuha desert there are significant
 219 deviations from the master curve for smaller arguments indicating that c varies with the
 220 magnitude of the trigger, similar to what has been observed for tectonic earthquakes in
 221 southern California (Davidsen & Baiesi, 2016).

222 4.4 Triggering topology

223 Going beyond first generation of aftershocks, we focus on full triggering cascades or
 224 aftershock sequences. An aftershock sequence starts with a single (background) event that
 225 triggers its first generation of aftershocks, which in turn trigger the next generation of
 226 aftershocks and so on. This corresponds to the topology of a rooted tree (Zaliapin & Ben-
 227 Zion, 2013). In this representation, the "leaf depth", d_f , refers to the minimum number of
 228 generations between a given leaf (an event in the aftershock sequence that does not trigger an
 229 event) and the tree root. Averaging d_f over all leaves in a given tree provides insight into the

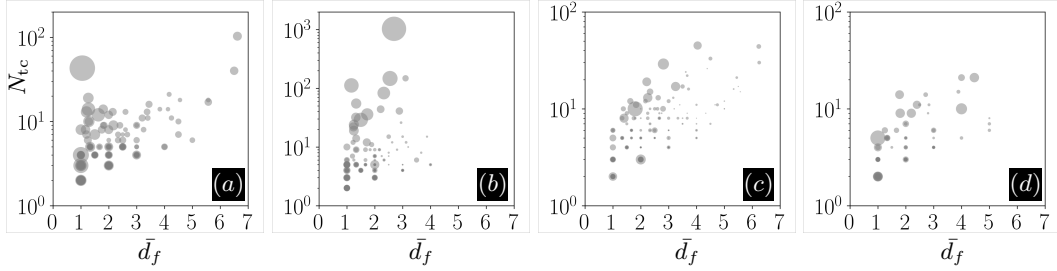


Figure 4. Number of events in the triggering cascade N_{tc} versus mean leaf depth \bar{d}_f in **a)** Oklahoma and southern Kansas **b)** the Yuha Desert **c)** Long Valley Caldera with $b = 0.7, m_c = 0.2$ **d)** Long Valley Caldera with $b = 0.9, m_c = 1.0$. Symbol sizes represent magnitudes of the root events. The magnitude of the smallest and largest event are **a)** 2.8 – 5.8 **b)** 1.0 – 5.7 **c,d)** 0.2 – 3.5. For the sake of clarity, a gray color scale is used indicating the relative density of overlapping data points.

230 shape of the triggering cascade. A large size (total number of events) of a triggering cascade
 231 N_{tc} associated with a small \bar{d}_f indicates a burst-like topology, while small N_{tc} associated
 232 with a large \bar{d}_f indicates a swarm-like topology. Figure 4(a-d) displays scatter plots of
 233 the relationship between \bar{d}_f and N_{tc} . Comparing the different catalogs, we can identify
 234 both opposing behaviors. For the Long Valley Caldera in Fig. 4(c,d), the values of N_{tc} are
 235 comparatively small but \bar{d}_f can take on relatively large values, while the Yuha Desert data
 236 show the opposite behavior. Thus, the natural swarm in the Long Valley Caldera tends to
 237 exhibit indeed a swarm-like topology, while the suspected swarms in the Yuha Desert tend to
 238 exhibit a more burst-like topology. Fig. 4(a) shows that the induced seismicity in Oklahoma
 239 and southern Kansas largely exhibits swarm-like behavior consistent with other findings for
 240 induced seismicity (Maghsoudi et al., 2018). However, the second largest aftershock sequence
 241 initiated by the largest event has almost exclusively first generation aftershocks representing
 242 a clear burst structure, consistent with the classical aftershock paradigm (Zaliapin & Ben-
 243 Zion, 2013). This triggering cascade and other exemplary ones are shown in Figs. S4-S6 in
 244 the SM.

245 5 Discussion

246 Our analysis of (suspected) fluid-induced seismicity in Oklahoma and southern Kansas,
 247 the Yuha Desert, and the Long Valley Caldera has shown the relevance of event-event trig-
 248 gering in all cases. Overall, this triggering obeys the GR relation, the aftershock productivity
 249 relation, the OU aftershock rate, and the scaling of the spatial aftershock zone with main
 250 shock magnitudes. Table 1 summarizes the relevant scaling relations and presents the esti-
 251 mated exponents based on our analysis and based on three independent studies, two of which
 252 probe aftershocks in natural swarms (Hainzl et al., 2013; Llenos & Michael, 2019) within
 253 the framework of the Epidemic-Type Aftershock-Sequence (ETAS) model, and the final one
 254 studies aftershocks in tectonic settings (Gu et al., 2013) using the same methodology we do.

255

256 There are a number of significant differences and commonalities in the scaling exponents
 257 that stand out. First, the aftershock productivity in Oklahoma and southern Kansas is high,
 258 $\alpha = 0.8$, and comparable to tectonic systems in southern California. All other catalogs have
 259 smaller values with the Long Valley Caldera having the lowest, $\alpha \approx 0.4$. Low α values were
 260 previously reported in a number of natural settings involving earthquake swarms, analogous
 261 to the Caldera region (Hainzl & Ogata, 2005). In addition, an ETAS-based study pertaining

Location (Year)	Type	Gutenberg-Richter		Productivity	Omori-Utsu	Linear Density	Rupture Size
		$N \propto 10^{-b(m-m_c)}$	m_c	$N_{as} \propto 10^{\alpha m}$	$\lambda(t) \propto t^{-p}$	$\rho(r) \propto r^{-\nu}$	$r_{rup} \propto 10^{\sigma m}$
		b		α	p	ν	σ
Oklahoma & southern Kansas (2014–2017)	Fluid Induced (Man-made)	1.65	2.8	0.8	1.0	2.9	0.5
Long Valley Caldera, California (2014 a)	Natural Swarm	0.7	0.2	0.4	0.9	2.9	0.36
Long Valley Caldera, California (2014 b)	Natural Swarm	0.9	1.0	0.48	0.9	2.9	0.36
Yuha Desert, California (2010)	Fluid Induced (Natural)	0.95	1.0	0.6	1.0	1.7	0.4
Western Bohemia, Europe (2000 & 2008) (Hainzl et al., 2013)	Natural Swarm	0.9 & 1.25	0.5	0.61 – 0.68	1.33 – 1.37	–	–
San Ramon, California (1970–2015) (Llenos & Michael, 2019)	Natural Swarm	0.85	2.0	0.65	1.12	–	–
Southern California (1984–2005) (Gu et al., 2013)	Tectonic	1.09	2.5	0.85 – 0.9	1.2 – 1.25	1.6	0.4

Table 1. Comparison between estimated parameters and scaling exponents associated with different seismic catalogs and settings.

262 to swarm activities in Arkansas (Llenos & Michael, 2013) (which resembles the setting in
 263 Oklahoma) found that natural fluid flows lead to a lower aftershock productivity prior to
 264 injection-induced activity, as evidenced by smaller numerical estimates for α as well as for
 265 the constant of proportionality in the productivity relation. This is consistent with our
 266 observations and studies of induced seismicity related to hydraulic fracturing (Maghsoudi
 267 et al., 2018) suggesting that α allows one to distinguish between natural and human-made
 268 seismic swarms.

269 Second, the spatial density of aftershocks $\rho(r)$ falls off rapidly in Oklahoma and southern
 270 Kansas as well as in the Long Valley Caldera ($\nu = 2.9$), contrasted by long-range behavior
 271 in the Yuha Desert and also southern California with $\nu < 2$. In tectonic settings, the
 272 slow inverse power-law behavior of the aftershocks density $\rho(r) \propto r^{-\nu}$ beyond the rupture
 273 length can be explained by non-local transfer of static (Coulomb) stress within the brittle
 274 crust (Moradpour et al., 2014; Hainzl et al., 2014; van der Elst & Shaw, 2015). Given
 275 comparable estimates of ν between southern California (Gu et al., 2013) and the Yuha
 276 Desert, it is likely that the event-event triggering in the Yuha Desert is also largely driven
 277 by static stress changes. The relevance of such a triggering mechanism is consistent with
 278 the findings of our topology-based analysis, since the emerging *burstiness* may indicate the
 279 non-local transfer of internal stress within a rigid elastic medium (Zaliapin & Ben-Zion,
 280 2013). On the other hand, our overall findings support that a rapid decay of the aftershock
 281 zone (with $\nu \approx 3$) is indicative of the dominant role of fluid migration. In particular, this
 282 mechanism might be relevant for induced events in Oklahoma and southern Kansas as well
 283 as for natural swarms in the Long Valley Caldera. Shelly et al. (2016) reported on the
 284 diffusive (and most likely localized) nature of the swarm propagation in the latter, which
 285 is another typical signature associated with various fluid-dominated contexts (Ruhl et al.,
 286 2016). In our study, swarm-like features were independently evidenced from the topology
 287 of triggering cascades in Caldera and (to a slightly lesser extent) Oklahoma.

288 Narrow aftershock zones for Oklahoma and southern Kansas were independently reported
 289 in (Rosson et al., 2019) based on a spatio-temporal windowing approach. Rosson et
 290 al. (2019) argued that the absence of long-range triggering might also be due to structural

291 heterogeneities within the fault network in Oklahoma and southern Kansas, which could
 292 substantially constrain inter-fault activation in the region (Alt & Zoback, 2016). Similar
 293 arguments were made in (Shelly et al., 2016) pointing to the complex fault geometry in
 294 Caldera, which potentially led to confined swarm activities in this natural setting. Alto-
 295 together, the complex interplay between fluid migration and local heterogeneities appear to
 296 control the spatial extent of aftershock triggering in Oklahoma as well as Caldera.

297 As for the Omori exponent, Table 1 shows that $p \approx 1$ appears to be a robust measure-
 298 ment although there is a slightly faster decay associated with natural swarms in Bohemia
 299 (Hainzl et al., 2013) and perhaps tectonic-based earthquakes in southern California, which
 300 is expected for strike-slip faulting (Tahir & Grasso, 2015). Despite being distinguishable
 301 in terms of spatial aftershocks densities and productivity, both Oklahoma and the Yuha
 302 Desert exhibit statistically similar temporal features. This is in line with recent observa-
 303 tions made by (Rosson et al., 2019) comparing the induced setting in Oklahoma with the
 304 tectonics-based seismicity in southern California. We note that the latter is known to have
 305 well-established seismic features (Gu et al., 2013), which are comparatively close to what we
 306 find for the Yuha Desert (Table 1). We observed analogous temporal properties between the
 307 Caldera and Oklahoma case studies that, along with spatial similarities, might be indicative
 308 of the swarm-type evolution in fluid-induced settings.

309 6 Conclusions

310 We have identified common features of event-event triggering between human-made and
 311 natural seismicity in fluid-driven contexts. Two natural case studies, Long Valley Caldera
 312 and the Yuha Desert, were used as benchmarks, in which the fluid migration was (partially)
 313 involved. We recovered essential features of natural swarm-like activities in injection-induced
 314 seismicity in Oklahoma and southern Kansas. Most remarkably, the “swarminess” mani-
 315 fested itself in narrow spatial aftershock zones and associated triggering topology that did
 316 not match tectonic mainshock-aftershock sequences in addition to the absence of Båth’s law.
 317 Finally, high aftershock productivity associated with human-made swarms appears to be a
 318 robust indicator making them distinguishable from naturally-induced swarms, which is of
 319 direct importance for earthquake forecasting and seismic hazard analysis.

320 Acknowledgments

321 Sponsors of the Microseismic Industry Consortium are sincerely thanked for their support
 322 of this initiative. This work was supported by funding from a Collaborative Research and
 323 Development grant from the Natural Sciences and Engineering Research Council of Canada.

324 Data Availability Statement

325 Datasets for this research are included in (Schoenball & Ellsworth, 2017a), (Ross et al.,
 326 2017), and (Shelly et al., 2016).

327 References

- 328 Alt, R. C., & Zoback, M. D. (2016). In situ stress and active faulting in Oklahoma. *Bulletin*
 329 *of the Seismological Society of America*, *107*(1), 216–228.
- 330 Baró, J., & Davidsen, J. (2017). Are triggering rates of labquakes universal? inferring
 331 triggering rates from incomplete information. *The European Physical Journal Special*
 332 *Topics*, *226*(15), 3211–3225.
- 333 Bhattacharya, P., Phan, M., & Shcherbakov, R. (2011). Statistical analysis of the 2002
 334 Mw 7.9 Denali earthquake aftershock sequence. *Bulletin of the Seismological Society*
 335 *of America*, *101*(6), 2662–2674.
- 336 Brengman, C. M., Barnhart, W. D., Mankin, E. H., & Miller, C. N. (2019). Earthquake-

- 337 scaling relationships from geodetically derived slip distributions. *Bulletin of the Seis-*
 338 *mological Society of America*, 109(5), 1701–1715.
- 339 Dascher-Cousineau, K., Brodsky, E. E., Lay, T., & Goebel, T. H. (2020). What controls
 340 variations in aftershock productivity? *Journal of Geophysical Research: Solid Earth*.
- 341 Davidsen, J., & Baiesi, M. (2016). Self-similar aftershock rates. *Physical Review E*, 94(2),
 342 022314.
- 343 Davidsen, J., Gu, C., & Baiesi, M. (2015). Generalized Omori–Utsu law for aftershock
 344 sequences in southern California. *Geophysical Journal International*, 201(2), 965–
 345 978.
- 346 Davidsen, J., Kwiatek, G., Charalampidou, E.-M., Goebel, T., Stanchits, S., Rück, M., &
 347 Dresen, G. (2017). Triggering processes in rock fracture. *Physical Review Letters*,
 348 119(6), 068501.
- 349 Deflandre, J.-P. (2016). Induced microseismicity: Short overview, state of the art and
 350 feedback on source rock production. *The Open Petroleum Engineering Journal*, 9(1).
- 351 Dinske, C., & Shapiro, S. A. (2013). Seismotectonic state of reservoirs inferred from mag-
 352 nitude distributions of fluid-induced seismicity. *Journal of seismology*, 17(1), 13–25.
- 353 Eaton, D. W., Davidsen, J., Pedersen, P. K., & Boroumand, N. (2014). Breakdown of
 354 the Gutenberg-Richter relation for microearthquakes induced by hydraulic fracturing:
 355 influence of stratabound fractures. *Geophysical Prospecting*, 62(VERTICAL Seismic
 356 Profiling and Microseismicity Frontiers), 806–818.
- 357 Eaton, D. W., & Maghsoudi, S. (2015). 2b... or not 2b? interpreting magnitude distributions
 358 from microseismic catalogs. *First Break*, 33(10), 79–86.
- 359 Ellsworth, W. L. (2013). Injection-induced earthquakes. *Science*, 341(6142), 1225942.
- 360 Eyre, T. S., Eaton, D. W., Garagash, D. I., Zecevic, M., Venieri, M., Weir, R., & Lawton,
 361 D. C. (2019). The role of aseismic slip in hydraulic fracturing-induced seismicity.
 362 *Science advances*, 5(8), eaav7172.
- 363 Gneiting, T., Ševčíková, H., & Percival, D. B. (2012). Estimators of fractal dimension:
 364 Assessing the roughness of time series and spatial data. *Statistical Science*, 247–277.
- 365 Goebel, T., Rosson, Z., Brodsky, E., & Walter, J. (2019). Aftershock deficiency of in-
 366 duced earthquake sequences during rapid mitigation efforts in Oklahoma. *Earth and*
 367 *Planetary Science Letters*, 522, 135–143.
- 368 Goebel, T. H., & Brodsky, E. E. (2018). The spatial footprint of injection wells in a global
 369 compilation of induced earthquake sequences. *Science*, 361(6405), 899–904.
- 370 Gu, C., Schumann, A. Y., Baiesi, M., & Davidsen, J. (2013). Triggering cascades and
 371 statistical properties of aftershocks. *Journal of Geophysical Research: Solid Earth*,
 372 118(8), 4278–4295.
- 373 Hainzl, S. (2016). Rate-dependent incompleteness of earthquake catalogs. *Seismological*
 374 *Research Letters*, 87(2A), 337–344.
- 375 Hainzl, S., Moradpour, J., & Davidsen, J. (2014). Static stress triggering explains the
 376 empirical aftershock distance decay. *Geophysical Research Letters*, 41(24), 8818–8824.
- 377 Hainzl, S., & Ogata, Y. (2005). Detecting fluid signals in seismicity data through statistical
 378 earthquake modeling. *Journal of Geophysical Research: Solid Earth*, 110(B5).
- 379 Hainzl, S., Zakharova, O., & Marsan, D. (2013). Impact of aseismic transients on the
 380 estimation of aftershock productivity parameters. *Bulletin of the Seismological Society*
 381 *of America*, 103(3), 1723–1732.
- 382 Kagan, Y. Y. (2013). *Earthquakes: models, statistics, testable forecasts*. John Wiley &
 383 Sons.
- 384 Kantz, H., & Schreiber, T. (2004). *Nonlinear time series analysis* (Vol. 7). Cambridge
 385 university press.
- 386 Langenbruch, C., & Zoback, M. D. (2016). How will induced seismicity in Oklahoma respond
 387 to decreased saltwater injection rates? *Science advances*, 2(11), e1601542.
- 388 Leonard, M. (2010). Earthquake fault scaling: Self-consistent relating of rupture length,
 389 width, average displacement, and moment release. *Bulletin of the Seismological Society*
 390 *of America*, 100(5A), 1971–1988.

- 391 Llenos, A. L., & Michael, A. J. (2013). Modeling earthquake rate changes in Oklahoma
392 and Arkansas: Possible signatures of induced seismicity. *Bulletin of the Seismological*
393 *Society of America*, *103*(5), 2850–2861.
- 394 Llenos, A. L., & Michael, A. J. (2019). Ensembles of etas models provide optimal operational
395 earthquake forecasting during swarms: Insights from the 2015 San Ramon, California
396 swarm. *Bulletin of the Seismological Society of America*, *109*(6), 2145–2158.
- 397 Maghsoudi, S., Baró, J., Kent, A., Eaton, D., & Davidsen, J. (2018). Interevent triggering in
398 microseismicity induced by hydraulic fracturing. *Bulletin of the Seismological Society*
399 *of America*, *108*(3A), 1133–1146.
- 400 Maghsoudi, S., Eaton, D. W., & Davidsen, J. (2016). Nontrivial clustering of microseismicity
401 induced by hydraulic fracturing. *Geophysical Research Letters*, *43*(20), 10–672.
- 402 Marsan, D., & Helmstetter, A. (2017). How variable is the number of triggered aftershocks?
403 *Journal of Geophysical Research: Solid Earth*, *122*(7), 5544–5560.
- 404 Marsan, D., & Lengline, O. (2008). Extending earthquakes’ reach through cascading.
405 *Science*, *319*(5866), 1076–1079.
- 406 Moradpour, J., Hainzl, S., & Davidsen, J. (2014). Nontrivial decay of aftershock density
407 with distance in southern California. *Journal of Geophysical Research: Solid Earth*,
408 *119*(7), 5518–5535.
- 409 Ross, Z. E., Rollins, C., Cochran, E. S., Hauksson, E., Avouac, J.-P., & Ben-Zion, Y. (2017).
410 Aftershocks driven by afterslip and fluid pressure sweeping through a fault-fracture
411 mesh. *Geophysical Research Letters*, *44*(16), 8260–8267.
- 412 Rosson, Z., Walter, J., Goebel, T., & Chen, X. (2019). Narrow spatial aftershock zones for
413 induced earthquake sequences in Oklahoma. *Geophysical Research Letters*, *46*(17-18),
414 10358–10366.
- 415 Ruhl, C., Abercrombie, R., Smith, K., & Zaliapin, I. (2016). Complex spatiotemporal
416 evolution of the 2008 Mw 4.9 Mogul earthquake swarm (Reno, Nevada): Interplay of
417 fluid and faulting. *Journal of Geophysical Research: Solid Earth*, *121*(11), 8196–8216.
- 418 Schoenball, M., Davatzes, N. C., & Glen, J. M. (2015). Differentiating induced and natural
419 seismicity using space-time-magnitude statistics applied to the Coso geothermal field.
420 *Geophysical Research Letters*, *42*(15), 6221–6228.
- 421 Schoenball, M., & Ellsworth, W. L. (2017a). A systematic assessment of the spatiotemporal
422 evolution of fault activation through induced seismicity in Oklahoma and southern
423 Kansas. *Journal of Geophysical Research: Solid Earth*, *122*(12).
- 424 Schoenball, M., & Ellsworth, W. L. (2017b). Waveform-relocated earthquake catalog for
425 Oklahoma and southern Kansas illuminates the regional fault network. *Seismological*
426 *Research Letters*, *88*(5), 1252–1258.
- 427 Scholz, C. H. (2019). *The mechanics of earthquakes and faulting*. Cambridge university
428 press.
- 429 Shapiro, S. A. (2015). *Fluid-induced seismicity*. Cambridge University Press.
- 430 Shelly, D. R., Ellsworth, W. L., & Hill, D. P. (2016). Fluid-faulting evolution in high
431 definition: Connecting fault structure and frequency-magnitude variations during the
432 2014 Long Valley Caldera, California, earthquake swarm. *Journal of Geophysical*
433 *Research: Solid Earth*, *121*(3), 1776–1795.
- 434 Skoumal, R. J., Brudzinski, M. R., & Currie, B. S. (2015). Distinguishing induced seismicity
435 from natural seismicity in Ohio: Demonstrating the utility of waveform template
436 matching. *Journal of Geophysical Research: Solid Earth*, *120*(9), 6284–6296.
- 437 Tahir, M., & Grasso, J. R. (2015). Faulting style controls for the space-time aftershock
438 patterns. *Bulletin of the Seismological Society of America*, *105*(5), 2480–2497.
- 439 Teng, G., & Baker, J. W. (2019). Seismicity declustering and hazard analysis of the
440 Oklahoma–Kansas region. *Bulletin of the Seismological Society of America*, *109*(6),
441 2356–2366.
- 442 Utsu, T., Ogata, Y., et al. (1995). The centenary of the Omori formula for a decay law of
443 aftershock activity. *Journal of Physics of the Earth*, *43*(1), 1–33.
- 444 van der Elst, N. J., & Shaw, B. E. (2015). Larger aftershocks happen farther away: Nonsep-
445 arability of magnitude and spatial distributions of aftershocks. *Geophysical Research*

- 446 *Letters*, 42(14), 5771–5778.
- 447 Vasylykivska, V. S., & Huerta, N. J. (2017). Spatiotemporal distribution of Oklahoma
448 earthquakes: Exploring relationships using a nearest-neighbor approach. *Journal of*
449 *Geophysical Research: Solid Earth*, 122(7), 5395–5416.
- 450 Zaliapin, I., & Ben-Zion, Y. (2013). Earthquake clusters in southern California ii: Classifica-
451 tion and relation to physical properties of the crust. *Journal of Geophysical Research:*
452 *Solid Earth*, 118(6), 2865–2877.
- 453 Zaliapin, I., Gabrielov, A., Keilis-Borok, V., & Wong, H. (2008). Clustering analysis of
454 seismicity and aftershock identification. *Physical Review Letters*, 101(1), 018501.